

Magnetism in $\text{La}_2\text{O}_3(\text{Fe}_{1-x}\text{Mn}_x)_2\text{Se}_2$ tuned by Fe/Mn ratio

Hechang Lei,¹ Emil S. Bozin,¹ A. Llobet,² V. Ivanovski,³ V. Koteski,³ J. Belosevic-Cavor,³ B. Cekic,³ and C. Petrovic¹

¹*Condensed Matter Physics and Materials Science Department,
Brookhaven National Laboratory, Upton, NY 11973 USA*

²*Lujan Neutron Scattering Center, Los Alamos National Laboratory,
MS H805, Los Alamos, New Mexico 87545, USA*

³*Institute of Nuclear Sciences Vinca, University of Belgrade, Belgrade 11001, Serbia*

(Dated: November 6, 2018)

We report the evolution of structural and magnetic properties in $\text{La}_2\text{O}_3(\text{Fe}_{1-x}\text{Mn}_x)_2\text{Se}_2$. Heat capacity and bulk magnetization indicate increased ferromagnetic component of the long range magnetic order and possible increased degree of frustration. Atomic disorder on Fe(Mn) sites suppresses the temperature of the long range order whereas intermediate alloys show rich magnetic phase diagram.

PACS numbers: 74.25.Wx, 74.25.F-, 74.25.Op, 74.70.Dd

I. INTRODUCTION

Parent materials of cuprates and iron-based superconductors are layered transition-metal compounds (TMP's) with antiferromagnetic (AFM) ground state due to a dissimilar magnetic mechanism and with rather different electronic conductivity.¹ Local environment of TM is intimately connected with this since puckering of iron pnictide crystallographic layers promotes higher conductivity in parent materials of iron superconductors, as opposed to cuprates.^{2,3} Recently, a family of layered TMP oxychalcogenides $\text{Ln}_2\text{O}_3\text{TM}_2\text{Ch}_2$ (Ln = rare earth, TM = transition metal, and Ch = S, Se) and its analogues $\text{A}_2\text{F}_2\text{TM}_2\text{OCh}_2$ (A = Sr, Ba)(2322) has received more attention.⁴⁻¹⁶ They have anti- CuO_2 -type $[\text{TM}_2\text{OCh}_2]^{2-}$ layers and the local environment of TM bears much more resemblance to manganites or cuprates than to iron based superconductors. This typically results in semiconducting or Mott insulating ground state with AFM transition.^{5,8} Within the $[\text{TM}_2\text{OCh}_2]^{2-}$ layers transition metal atoms are located at the distorted octahedral environment due to the different distances of TM-Ch and TM-O, whereas the TM-Ch(O) octahedrons are face sharing. This distortion lifts the degeneracy of e_g and t_{2g} levels in a non-distorted octahedral crystal field. The $[\text{TM}_2\text{OCh}_2]^{2-}$ layers in the crystal structure harbor three principal competing interactions: the nearest neighbor (NN) J_3 interaction of the closest TM atoms in the crystallographic ab plane, next nearest neighbor (NNN) superexchange interaction J_2 of nearly 90° TM-Ch-TM, and (NNN) J_1 superexchange interaction of 180° TM-O-TM.^{4,6,8,14} Theoretical calculation and neutron diffraction results indicate that the AFM transition stems from the competition of three interactions in an unusual frustrated AFM checkerboard spin-lattice system.^{6-10,14,16} Frustrated magnetic order on checkerboard lattices hosts rich magnetic ground states and could be relevant to physics of colossal magnetoresistance manganites and iron based and cuprates superconducting materials.¹⁷⁻²¹ Therefore it is of interest to address the nature of magnetic order and frustration in 2322 materials since it

shares some characteristics of all the above mentioned compounds.

Among 2322 materials, $\text{La}_2\text{O}_3\text{Mn}_2\text{Se}_2$ (Mn-2322) exhibits a faint specific heat anomaly at AFM transition and two dimensional (2D) short range magnetic correlations that lock magnetic entropy far above the temperature of the bulk long range AFM transition.^{14,15} Weak ferromagnetic (FM) component superimposed on the paramagnetic background in $M(H)$ loops at 2 K proposed to arise due to spin reorientation and/or spin canting below the AFM transition,¹⁴ might also come from magnetic impurities such as Mn_3O_4 .¹⁶ Mn-2322 has a G-type AFM structure with the ordered moment along the c axis direction and where NN Mn ions have opposite spins with dominant AFM $J_3 < 0$ and fully frustrated $|J_1| < J_2$ with $J_1 < 0$ and $J_2 > 0$.^{14,16} On the other hand, $\text{La}_2\text{O}_3\text{Fe}_2\text{Se}_2$ (Fe-2322) adopts magnetic structure similar to FeTe where half of the J_3 , J_2 and J_1 are frustrated^{9,16,22} and different from the theoretical predictions.⁸ This is different from other compounds with same structure, in which J_1 is the dominant term.¹⁰

In this work we tuned the magnetism on Fe/Mn checkerboard lattice by varying TM content and examined the magnetic ground states of $\text{La}_2\text{O}_3(\text{Fe}_{1-x}\text{Mn}_x)_2\text{Se}_2$ series. We find that Mn substitution lead to the increase of activation energies for the electrical transport energy gap E_a and has strong effect on magnetic phase diagram and the spin entropy release above the temperature of the long range magnetic order.

II. EXPERIMENT

$\text{La}_2\text{O}_3(\text{Fe},\text{Mn})_2\text{Se}_2$ ((Fe,Mn)-2322) polycrystals were synthesized by solid state reaction from high purity materials ($\geq 99\%$). Dried La_2O_3 powder, Mn lump, Fe and Se powders were mixed and ground in an agate mortar. The mixture was pressed into pellets and sealed in a quartz tube backfilled with pure Argon gas. The ampule was heated to 1273 K and reacted for 24 h followed by furnace cooling. This was repeated several times to en-

sure homogeneity. The color of final product is yellowish green for Mn-2323 and black for Fe-2322.

Powder X-ray diffraction (XRD) patterns of the ground samples were taken with Cu K_{α} = 0.1458 nm using a Rigaku Miniflex X-ray machine. The structural parameters were obtained by Rietveld refinement using RIETICA software.²³ Single crystal X-ray data were collected in a Bruker Kappa Apex II single crystal X-ray diffractometer at the room temperature with Mo K_{α} = 0.071073 nm on a 20 μ m single crystal isolated from the polycrystalline powder. Single crystal unit cell refinement was performed with Bruker APEX 2 software package. Time-of-flight neutron diffraction measurements were carried out at 300 K on the high intensity powder diffractometer (HIPD) of the Lujan Neutron Scattering Center at the Los Alamos National Laboratory. Pulverized samples were loaded in extruded vanadium containers in helium atmosphere and sealed. Data were collected for 1 hour for each sample. Rietveld refinements of the data were carried out using GSAS software^{24,25} within the I4/mmm space group.

Mössbauer spectra were taken in transmission mode with $^{57}\text{Co}(\text{Rh})$ source at 294 K and the parameters were obtained using WinNormos software.²⁶ Calibration of the spectrum was performed by laser and isomer shifts were given with respect to α -Fe.

Thermal, transport and magnetic measurements were carried out in a Quantum Design PPMS-9 and MPMS-5. The samples were cut into rectangular parallelepipeds and thin Pt wires were attached for four probe resistivity measurements. Sample dimensions were measured with an optical microscope Nikon SMZ-800 with 10 μ m resolution.

III. RESULTS AND DISCUSSIONS

Crystal structure of (Fe,Mn)-2322 and principle magnetic interactions J_1 - J_3 are shown in Fig. 1(a,b). Both XRD and neutron reflections can be indexed using a tetragonal unit cell (Fig. 1(c,d)), indicating a continuous solid solution between Mn-2322 and Fe-2322. Unit cell of Mn-2322 single crystal determined from the single crystal X-ray experiment was I4/mmm with a = 0.417(3) nm and c = 1.89(2) nm, in agreement with the powder data. Powder X-ray and neutron lattice parameters are shown in Fig. 1(e) and details of the crystal structure extracted from the neutron data, listed in Tables I-III, are consistent with the reported values.^{8,14} For Mn-2322, using obtained Mn-Se and Mn-O bond lengths (shown in Table 1), we calculate the valence of Mn ions using the bond valence sum (BVS) formalism in which each bond with a distance d_{ij} contributes a valence $v_{ij} = \exp[(R_{ij} - d_{ij})/0.37]$ with R_{ij} as an empirical parameter and the total of valences of atom i, V_i equals $V_i = \sum_j v_{ij}$.^{27,28} The calculated valence of Mn ions is +2.03, consistent with the apparent oxidation state (+2)

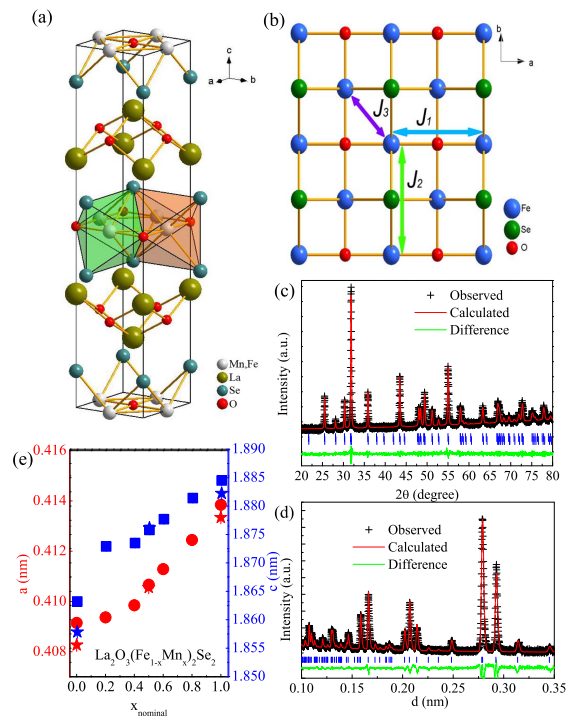


FIG. 1. (a) Crystal structure of (Fe,Mn)-2322. (b) TM-O planes shown for TM = Fe. Se atoms (green) are puckered above and below the plane, with Se-Fe-Se angle 97.04° along both a and b crystallographic axes. (c) and (d) XRD and neutron powder diffraction results at room temperature for the Mn-2322 polycrystal, respectively. (e) Lattice parameters for (Fe,Mn)-2322 determined from neutron diffraction (stars) and XRD (circles).

for Mn atoms. With increase in Mn content, the lattice parameters increase gradually for both a and c axes, hence the unit cell of Mn-2322 is larger than Fe-2322, which itself is larger than the unit cell of $\text{La}_2\text{O}_2\text{Co}_2\text{OSe}_2$ (Co-2322).^{4,7} This trend can be explained by the larger ionic size of Mn^{2+} when compared to Fe^{2+} and Co^{2+} ions, giving some insight in the spin state of Mn^{2+} ions. The lattice parameters should be proportional to the ionic size, $r_{\text{TM}^{2+}}$, of transition metals TM^{2+} (TM = Mn, Fe, and Co). Therefore from the observation $a_{\text{Mn}} = 0.41334 \text{ nm} > a_{\text{Fe}} = 0.40788 \text{ nm} > a_{\text{Co}} = 0.40697 \text{ nm}$ and $c_{\text{Mn}} = 1.88221 \text{ nm} > c_{\text{Fe}} = 1.86480 \text{ nm} > c_{\text{Co}} = 1.84190 \text{ nm}$ we conclude that $r_{\text{Mn}^{2+}} > r_{\text{Fe}^{2+}} > r_{\text{Co}^{2+}}$. Mössbauer spectra and theoretical calculations for Fe-2322 and Co-2322 suggest that Fe^{2+} and Co^{2+} are in the high spin state.^{6,10} This is in agreement with $r_{\text{Fe}^{2+}}(0.0780 \text{ nm}) > r_{\text{Co}^{2+}}(0.0745 \text{ nm})$ for high spin (HS) state (coordination number = 6). Therefore, the Mn^{2+} ions should be in the HS state since $r_{\text{Mn}^{2+}}(\text{LS}) = 0.067 \text{ nm}$ (LS = low spin) and $r_{\text{Mn}^{2+}}(\text{HS}) = 0.083 \text{ nm}$ for Mn^{2+} with 6-fold coordination.

TABLE I. Structural parameters for $\text{La}_2\text{O}_3\text{Fe}_2\text{Se}_2$ at 300 K.

Chemical Formula		$\text{La}_2\text{O}_3\text{Fe}_2\text{Se}_2$			
Interatomic Distances (nm)		Bond Angles ($^\circ$)			
$d_{\text{Fe-O}}$	0.20413(1)	O-Fe-O	180		
$d_{\text{Fe-Se}}$	0.27129(8)	Se-Fe-Se	97.61(4)/82.39(4)		
$d_{\text{Fe-Fe}}$	0.28869(1)	Se-Fe-O	90		
Atom	x	y	z	Occ	U_{iso} (10^{-2}nm^2)
La	0.5	0.5	0.1843(1)	1	0.0026(2)
O1	0.5	0	0.25	1	0.0059(3)
O2	0.5	0.5	0	1	0.0124(5)
Fe	0.5	0	0	1	0.0059(2)
Se	0	0	0.0962(1)	1	0.0032(2)

TABLE II. Structural parameters for $\text{La}_2\text{O}_3(\text{Fe}_{0.5}\text{Mn}_{0.5})_2\text{Se}_2$ at 300 K.

Chemical Formula		$\text{La}_2\text{O}_3(\text{Fe}_{0.5}\text{Mn}_{0.5})_2\text{Se}_2$			
Interatomic Distances (nm)		Bond Angles ($^\circ$)			
$d_{\text{Fe/Mn-O}}$	0.20528(1)	O-Fe-O	180		
$d_{\text{Fe/Mn-Se}}$	0.27641(12)	Se-Fe-Se	95.92(6)/84.08(6)		
$d_{\text{Fe/Mn-Fe/Mn}}$	0.29031(1)	Se-Fe/Mn-O	90		
Atom	x	y	z	Occ	U_{iso} (10^{-2}nm^2)
La	0.5	0.5	0.1851(1)	1	0.0057(3)
O1	0.5	0	0.25	1	0.0051(5)
O2	0.5	0.5	0	1	0.0100(7)
Fe	0.5	0	0	1	0.0058(8)
Se	0	0	0.0987(1)	1	0.0044(4)

TABLE III. Structural parameters for $\text{La}_2\text{O}_3\text{Mn}_2\text{Se}_2$ at 300 K.

Chemical Formula		$\text{La}_2\text{O}_3\text{Mn}_2\text{Se}_2$			
Interatomic Distances (nm)		Bond Angles ($^\circ$)			
$d_{\text{Mn-O}}$	0.2667(1)	O-Mn-O	180		
$d_{\text{Mn-Se}}$	0.28030(1)	Se-Mn-Se	95.01(1)/84.99(1)		
$d_{\text{Mn-Mn}}$	0.29227(1)	Se-Fe-O	90		
Atom	x	y	z	Occ	U_{iso} (10^{-2}nm^2)
La	0.5	0.5	0.1866(2)	1	0.0042(5)
O1	0.5	0	0.25	1	0.0057(7)
O2	0.5	0.5	0	1	0.0015(8)
Mn	0.5	0	0	1	0.0086(8)
Se	0	0	0.1006(1)	1	0.0020(5)

TABLE IV. Mössbauer isomer shifts δ and electric field quadrupole splittings ΔE_Q for $\text{La}_2\text{O}_3(\text{Fe}_{1-x}\text{Mn}_x)_2\text{Se}_2$ at 294 K.

Chemical formula	δ (mm/s)	ΔE_Q (mm/s)	Γ (mm/s)
$\text{La}_2\text{O}_3\text{Fe}_2\text{Se}_2$	0.895(1)	1.952(1)	0.287(2)
$\text{La}_2\text{O}_3(\text{Fe}_{0.8}\text{Mn}_{0.2})_2\text{Se}_2$	0.90(4)	1.756	0.309
$\text{La}_2\text{O}_3(\text{Fe}_{0.5}\text{Mn}_{0.5})_2\text{Se}_2$	0.812(6)	1.60(1)	0.309(7)

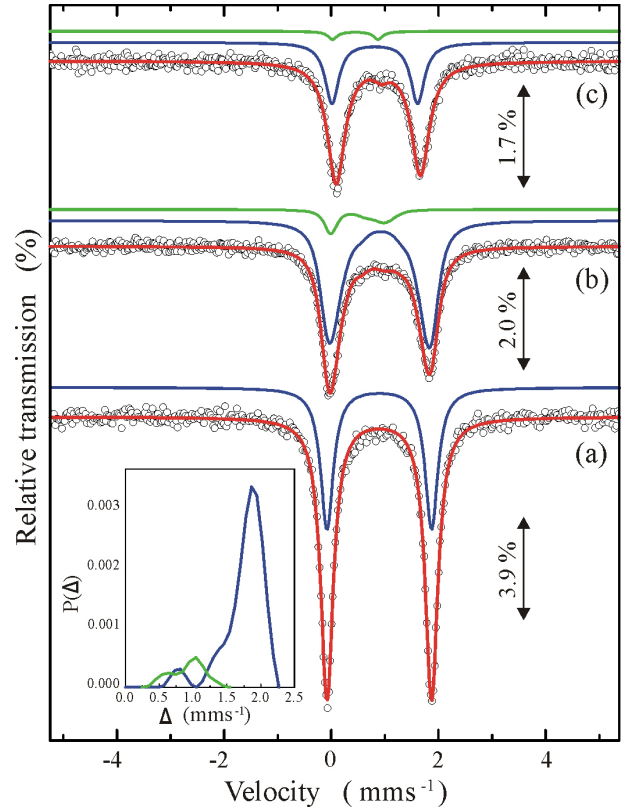


FIG. 2. Mössbauer spectra of $\text{La}_2\text{O}_3(\text{Fe}_{1-x}\text{Mn}_x)_2\text{Se}_2$ for $x = 0$ (a), $x = 0.2$ (b), and $x = 0.5$ (c), respectively. Vertical arrows denote relative positions of peaks with respect to the background. The data were shown by open circles and the fit is given by the red solid line. The doublets of the main (blue) and impurity (green) phases are offset for clarity. Inset shows the distributions of the electrical quadrupole splitting at the ^{57}Fe spectrum of $\text{La}_2\text{O}_3(\text{Fe}_{0.8}\text{Mn}_{0.2})_2\text{Se}_2$.

Mössbauer isomer shifts δ are sensitive on the electron density on a nucleus. Electric quadrupole splitting Δ arises due to interaction between electric field gradient and nuclear quadrupole moment. The δ and Δ provide information of the oxidation, spin state, chemical bonding and site symmetry. Mössbauer spectra of Fe-^{2322} (Fig. 2(a)) shows a single doublet, consistent with a single inequivalent 4c position of Fe in $I4/mmm$ space group of the unit cell. Isomer shifts $\delta = 0.895(1)$ mm/s and quadrupole splitting ($\Delta = 1.952(1)$ mm/s) are well in agreement with the high spin $S = 2$ of Fe^{2+} in the D_{2h} symmetry site of FeO_2Se_2 octahedra.¹¹ However, the $v = 0.3$ mm/s discrepancy between the experimental and theoretical fits and the mild asymmetry of peak intensities suggest that another interaction is superimposed on the main doublet. The Fe^{2+} experiences either an additional doublet or sextet due to an impurity phase or a high temperature magnetism in the sample with magnetic dipole interaction of $\mu_0 H \ll eV_{zz}Q$ magnitude. However, no known impurity phase, including LaFeO_3 was able to explain the experimental spectra. In contrast, Mössbauer spectra in both $\text{La}_2\text{O}_3(\text{Fe}_{0.5}\text{Mn}_{0.5})_2\text{Se}_2$

and $\text{La}_2\text{O}_3(\text{Fe}_{0.8}\text{Mn}_{0.2})_2\text{Se}_2$ detected Fe-Se phase impurity with $\delta = 0.45(7)$ mm/s, $\Delta = 0.8(1)$ mm/s. When Mn substitutes Fe in 1:4 ratio (Fig. 2(b)) there are 8 Fe^{2+} ions in the first two coordination spheres which contribute to 10 different combinations after the substitution if all combinations are of equal probability. The most important contribution to hyperfine interactions is from the first coordination sphere. With 1:4 Mn to Fe ratio there are 3 different combinations: with 0, 1 or 2 Mn on four Fe sites. The ratio of these combinations is 17:20:3 respectively. Distribution of electric quadrupole splittings centered at 1.756 mm/s, with 0.309 mm/s standard deviation and pronounced tail near the smaller values confirms uniform distribution of Mn. The main doublet and minority phase (or interaction) are also present when one half of Fe^{2+} is replaced by Mn^{2+} in $\text{La}_2\text{O}_3(\text{Fe}_{0.5}\text{Mn}_{0.5})_2\text{Se}_2$ (Fig. 2(c)). The atomic positions where half of Fe ions were substituted by Mn are symmetric within the first coordination sphere around Fe^{2+} that contains FeO_2Se_2 and four closest Fe ions in the Fe-O planes (Fig. 1(a)). This is confirmed by the rather small widening of the doublet lines ($\Gamma = 0.309(7)$ mm/s). Decreased values of isomer shift δ suggest a change in the charge density on the Fe^{2+} and substantial decrease of the octahedra.⁴

In order to complement the Mössbauer measurements, we performed density functional theory (DFT) calculations using the WIEN2K all-electron full-potential APW+lo code.²⁹ For La, Fe, Mn, Se, and O atoms the muffin-tin sphere radii were set to 2.38, 1.86, 1.86, 2.5 and 1.62 a.u.. The basis set functions were expanded up to $R_{mt}K_{max} = 7$. We used the LDA-Fock-0.25 hybrid functional,^{10,30} which provides a viable alternative to the LDA+U approach in describing the electron correlations in this system. Starting from the Fe-2322 and Mn-2322 pure structures, we constructed $2 \times 2 \times 1$ supercells of $\text{La}_2\text{O}_3(\text{Fe}_{0.25}\text{Mn}_{0.75})_2\text{Se}_2$, $\text{La}_2\text{O}_3(\text{Fe}_{0.5}\text{Mn}_{0.5})_2\text{Se}_2$ and $\text{La}_2\text{O}_3(\text{Fe}_{0.75}\text{Mn}_{0.25})_2\text{Se}_2$ to approximate the mixed Fe-Mn systems. Figure 3 shows the total density of states (DOS) as calculated for the FM state of the investigated compounds.

The LDA-Fock-0.25 hybrid functional calculations correctly predict the Mott-insulating behavior of (Fe, Mn)-2322. The band gaps are similar but decrease somewhat from pure Fe-2322 (about 0.4 eV) to pure Mn-2322 (about 0.25 eV). The overall shape of the DOS across this group is very similar, one significant distinction being the band gap shift of the minority DOS towards lower energies with increased Mn content. In our checkerboard AFM LDA-Fock-0.25 calculations (carried out only for the end compounds, not shown here), the band gaps of Fe-2322 and Mn-2322 are found to be 1.85 and 0.99 eV, respectively. Our calculations indicate that the AFM state is more stable than the FM state by 0.75 eV in Fe-2322 and 0.43 eV in Mn-2322. The supercell approach also enabled us to calculate the electric field gradient (EFG) and isomer shift (IS) at Fe situated in several different local coordinations. In Figure 4 we com-

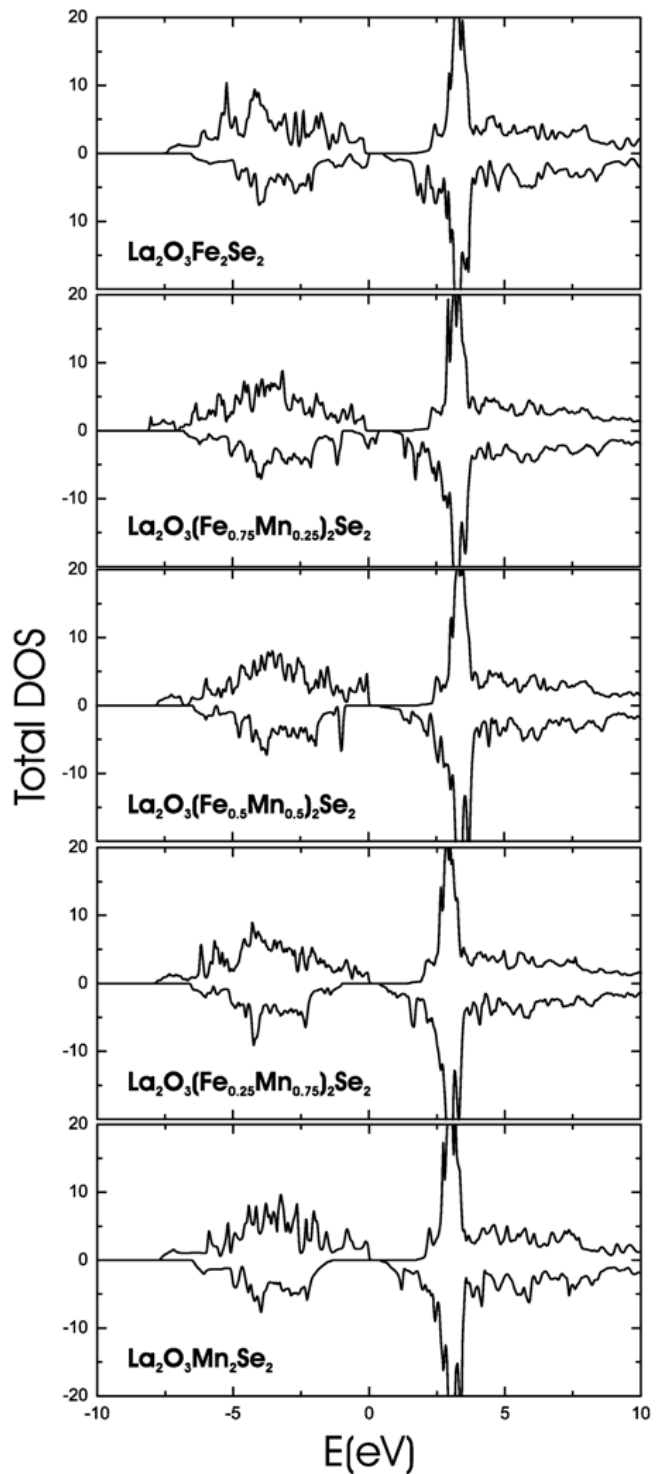


FIG. 3. Total DOS per formula unit for the FM state of (Fe, Mn)-2322. The Fermi level is set to zero energy. There is a band gap shift of the minority DOS towards lower energies as Mn substitutes Fe in the lattice.

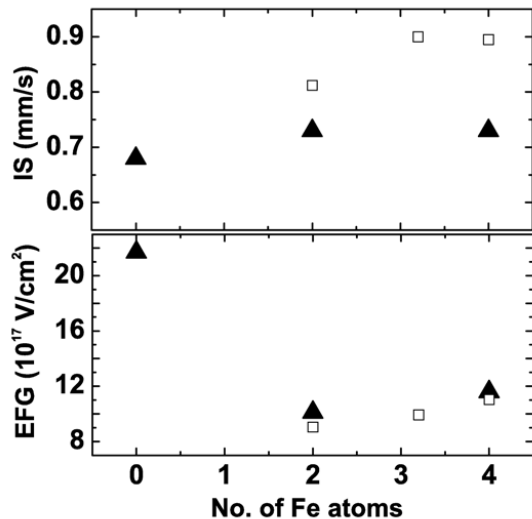


FIG. 4. Calculated (solid triangles) and measured (open squares) EFGs and ISs plotted as a function of the number of (in-plane) neighboring Fe atoms. Our $2 \times 2 \times 1$ supercells did not allow for geometries with 1 and 3 Fe atoms. The experimental EFGs and ISs are plotted against the average number of neighboring Fe atoms in $\text{La}_2\text{O}_3(\text{Fe}_{0.5}\text{Mn}_{0.5})_2\text{Se}_2$, $\text{La}_2\text{O}_3(\text{Fe}_{0.8}\text{Mn}_{0.2})_2\text{Se}_2$ and Fe-2322.

pare the results of our calculations with the values extracted from Mössbauer spectroscopy. While our calculations were able to reproduce the values of the measured EFGs, the ISs are found to be smaller than the experimental values by up to 20 percent. The discrepancy is because experimental Mössbauer includes second order Doppler shift and chemical isomer shift due to electronic density whereas the theoretical parts involves only the latter. The calculated EFG of 11.6×10^{21} V/m² in pure Fe-2322 agrees very well with the EFG obtained in similar DFT calculations.³¹

Neglecting grain boundaries, Mn-2322 resistivity at room temperature is about $2 \times 10^4 \Omega \cdot \text{cm}$. This is two orders of magnitude smaller than Co-2322.⁷ The resistivities of (Fe,Mn)-2322 exhibit activated behavior, $\rho = \rho_0 \exp(E_a/k_B T)$, where ρ_0 is the prefactor, E_a is the activation energy, k_B is the Boltzmann's constant and T is temperature (Fig. 5(a) and (b)). By fitting the $\rho(T)$ data from 210 to 320 K we obtain the activation energy $E_a = 0.2425(2)$ eV for Mn-2322. This is substantially smaller than the activation energy of Co-2322⁷ and consistent with the recently reported value.¹⁶ The E_a decreases rapidly by $x = 0.5$ (0.1814(3) eV), then gradually as the Mn/Fe ratio is tuned to Fe-2322 (0.1796(3) eV). The value of E_a for Fe-2322 is close to that reported in the literature.⁸ The residual resistivity values (ρ_0) exhibit the same trend. These results indicate that the band gap of (Fe,Mn)-2322 decreases with the contraction of lattice parameters. The narrowing of band gap is also consistent with sample color changes from yellowish green in Mn-2322 to black in Fe-2322. Gap values obtained for

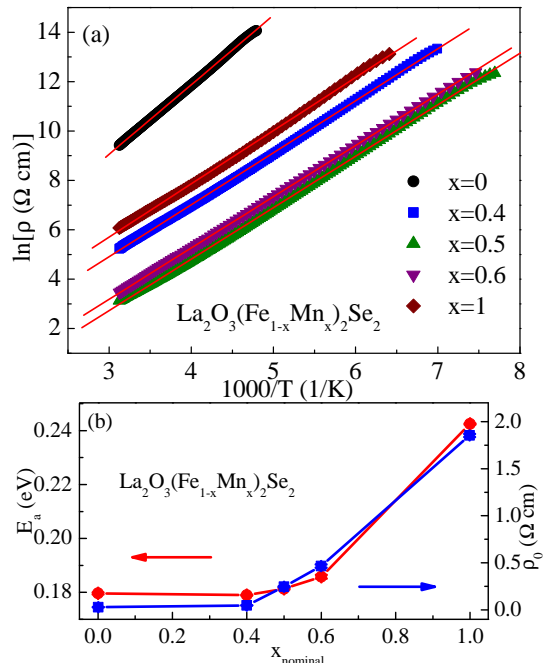


FIG. 5. (a) Temperature dependence of the resistivity for (Fe,Mn)-2322 polycrystals. (b) Activation energies using $\rho = \rho_0 \exp(E_a/k_B T)$ and the relation between ρ_0 , E_a and x_{nominal} .

Mn-2322 are in agreement with LDA calculations (Fig. 3), however for Fe-2322 and for intermediate alloys there is a disagreement. This suggests increased importance of strong electronic correlations for increased Fe site occupancy of Fe/Mn site in (Fe, Mn)-2322 alloys.

Temperature dependence of dc magnetic susceptibility $\chi(T) = M/H$ taken in 50 kOe magnetic field for (Fe,Mn)-2322 with zero field cooling (ZFC) is shown in Fig. 6(a). For Fe-2322, there is AFM transition at $T_N = 90$ K, consistent with previous results.⁸ With Mn doping, this AFM transition shifts to lower temperature quickly and disappears in Mn-2322. On the other hand, there is other FM-like transition emerging and shifting to higher temperature when Mn enters the lattice. Finally, for Mn-2322, The $\chi(T)$ curves of Mn-2322 (inset of Fig. 6(a)) exhibit three features: one broader maximum, T_{Max} and two anomalies, T_{M1} and T_{M2} . T_{Max} (~ 275 K) with no Curie-Weiss behavior up to 350 K implies that there is a stronger two-dimensional short-range spin correlations in Mn-2322 than in Fe-2322 at high temperature, reflecting the frustrated nature of the magnetic structure in Mn-2322.^{14,16} From the sharp minimum of the $d(\chi T)/dT$ curves (Fig. 6(b)) we extract $T_{M1} \sim 164$ K, in agreement with previous results.¹⁴⁻¹⁶ The T_{M1} anomaly is field independent and therefore should have considerable ferromagnetic component due to canting and/or magnetocrystalline anisotropy possibly induced by frustration.¹⁴ The second anomaly (minimum in $d(\chi T)/dT$ at $T_{M2} = 122$

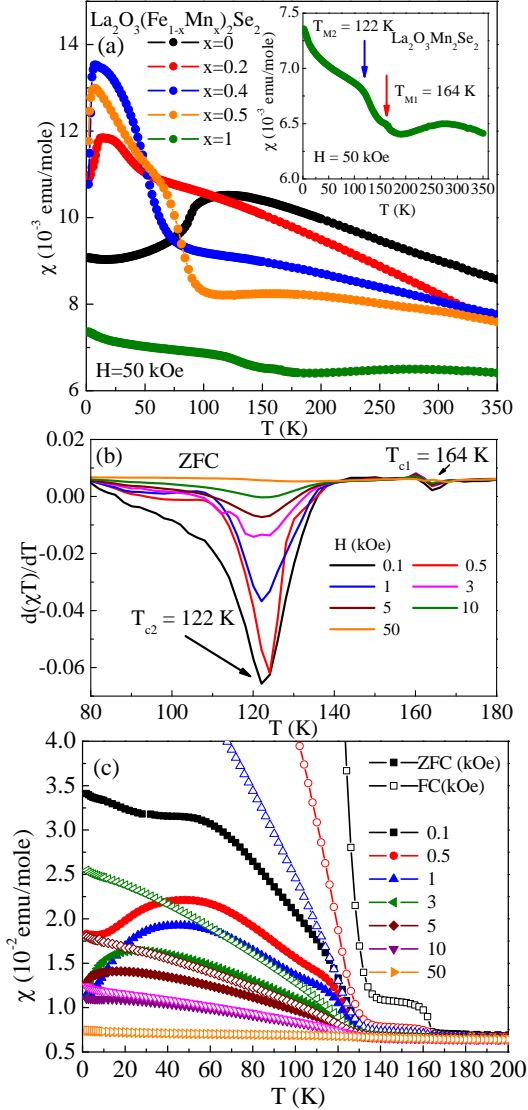


FIG. 6. (a) Temperature dependence of the magnetic susceptibility $\chi(T)$ for (Fe,Mn)-2322 taken in 50 kOe. Inset shows enlarged $\chi(T)$ for Mn-2322. (b) $d(\chi T)/dT$ of Mn-2322 at various magnetic fields for ZFC magnetization. (c) ZFC and FC curves of Mn-2322 near magnetic transitions.

K (inset of Fig. 6(a)) is also field independent, however it is strongly suppressed in high fields. This is in agreement with its proposed spin reorientation origin.¹⁴ The ZFC and field cooling (FC) $\chi(T)$ curves split at $T_{M1,2}$ but gradually overlap with magnetic field increase (Fig. 6(c)). This implies the presence of either magnetic frustration or magnetocrystalline anisotropy. On the other hand, $\chi(T)$ of Mn-2322 show a hump around $T_N = 42$ K at 1 kOe with ZFC mode (blue curve), similar to previous results.^{14,16} It could be due to superparamagnetic Mn_3O_4 nanoparticles contamination below our diffraction resolution limit.¹⁶ Overall, the substantial shift of

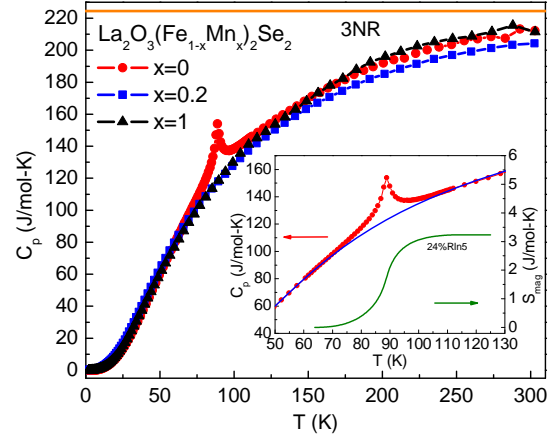


FIG. 7. Temperature dependence of specific heat for (Fe,Mn)-2322 polycrystals. Inset shows the specific heat of Fe-2322 data between 50 K and 130 K. The solid curve represents the phonon contribution fitted by a polynomial. The right axis and its associated solid curve denote the magnetic entropy related to the AFM transition of Fe-2322.

the cusp with x and evolution of FM-like increase of magnetization above the cusp temperature points to development of intrinsic magnetic interactions from Fe-2322 to Mn-2322. With Mn doping, the part of magnetic entropy that contributes to long range order rapidly shifts to lower temperature whereas frustration-induced FM (or canting, anisotropic exchange interactions) component of magnetization increases and high temperature two-dimensional short range magnetic order becomes stronger as the magnetic system is tuned toward the lattice with full Mn occupation.

Specific heat of (Fe,Mn)-2322 (Fig. 7) approaches the value of $3NR$ at 300 K, where N is the atomic number in the chemical formula ($N = 9$) and R is the gas constant ($R = 8.314 \text{ J mol}^{-1} \text{ K}^{-1}$), consistent with the Dulong-Petit law. On the other hand, Fe-2322 specific heat shows a λ -type anomaly at $T = 89$ K for Fe-2322 in agreement with the result in the literature.¹¹ This anomaly is due to a long-range 3D antiferromagnetic (AFM) ordering of the Fe^{2+} . After subtraction of the phonon contribution (C_{ph}) fitted using a polynomial for the total specific heat, we obtain the magnetic contribution (C_{mag}) and calculate the magnetic entropy using $S_{mag}(T) = \int_0^T C_{mag}/T dt$. The derived S_{mag} is 3.23 J/mol-K at 120 K, which is much smaller than the expected value ($\sim 24\% R \ln(2S + 1) = R \ln 5$) for Fe^{2+} ions with high spin state (inset of Fig. 7). Note that only about half of that value is released below T_N . It suggests that substantial fraction of magnetic entropy is locked at high temperatures due to possible 2D short-range magnetic order before long range correlations develop at T_N .¹⁴ In contrast, there is no λ -type anomaly for Mn-2322 at the temperature of magnetic transitions

($T_{M1} = 164$ K and $T_{M2} = 122$ K), which is consistent with the previous result and can be ascribed to the overwhelming release of magnetic entropy due to existence of 2D short-range order above magnetic transitions.¹⁴ The 20% Mn doping in Fe-2322 has already resulted in complete release of magnetic entropy above T_N . If the entropy is released via the high temperature frustration mechanism, this suggests that frustration effects are considerably enhanced with Mn doping. This could explain the absence of Curie-Weiss law in $M(T)$ above T_N (Fig. 6(a)).

IV. CONCLUSION

$\text{La}_2\text{O}_3(\text{Fe}_{1-x}\text{Mn}_x)_2\text{Se}_2$ compounds are magnetic with the high spin state for $\text{Fe}^{2+}/\text{Mn}^{2+}$. Intermediate alloys exhibit long range magnetic order and release magnetic entropy at high temperature due to possible magnetic frustration. Further neutron scattering experiments are necessary to provide microscopic information on how principle competing interactions evolve in this alloy series. FM component of magnetically ordered ground state and possibly the degree of magnetic frustration

both raise rapidly as Mn enters the lattice. In (Fe,Mn)-2322 compounds long range magnetic order competes with disorder induced by geometric spin frustration. Atomic disorder on Fe/Mn sites tips this balance and promotes frustration. Since the balance of all 3 principle interactions J_1 - J_3 can be tuned by Fe/Mn ratio, this system might be mapped to the 2D pyrochlore where charge order and metal to insulator transition have been predicted at half filling.^{32,33}

V. ACKNOWLEDGEMENTS

The part of this work was carried out at BNL which is operated for the U.S. Department of Energy by Brookhaven Science Associates under grant DE-AC02-98CH10886. A portion of this work was benefited from the use of HIPD at the Lujan Center at Los Alamos Neutron Science Center, funded by DOE Office of Basic Energy Sciences. Los Alamos National Laboratory is operated by Los Alamos National Security LLC under DOE Contract No. DE-AC52-06NA25396. This work has also been supported by the grant No. 45018 from the Serbian Ministry of Education and Science.

-
- ¹ I. I. Mazin, *Nature* **464**, 183 (2010).
² V. Cvetkovic and Z. Tesanovic, *Europhys. Lett* **85**, 37002 (2009).
³ M. M. Qazilbash, J. J. Hamlin, R. E. Baumbach, L. Zhang, D. J. Singh, M. B. Maple and D. N. Basov, *Nature Phys.* **5**, 647 (2009).
⁴ J. M. Mayer, L. F. Schneemeyer, T. Siegrist, J. V. Waszczak and B. Van Dover, *Angew. Chem., Int. Ed. Engl.* **31**, 1645 (1992).
⁵ S. J. Clarke, P. Adamson, S. J. C. Herkelrath, O. J. Rutt, D. R. Parker, M. J. Pitcher and C. F. Smura, *Inorg. Chem.* **47**, 8473 (2008).
⁶ H. Kabbour, E. Janod, B. Corraze, M. Danot, C. Lee, M. H. Whangbo and L. Cario, *J. Am. Chem. Soc.* **130**, 8261 (2008).
⁷ C. Wang, M. Q. Tan, C. M. Feng, Z. F. Ma, S. Jiang, Z. A. Xu, G. H. Cao, K. Matsubayashi and Y. Uwatoko, *J. Am. Chem. Soc.* **132**, 7069 (2010).
⁸ J. X. Zhu, R. Yu, H. Wang, L. L. Zhao, M. D. Jones, J. Dai, E. Abrahams, E. Morosan, M. Fang and Q. Si, *Phys. Rev. Lett.* **104**, 216405 (2010).
⁹ D. G. Free and J. S. O. Evans, *Phys. Rev. B* **81**, 214433 (2010).
¹⁰ H. Wu, *Phys. Rev. B* **82**, 020410 (2010).
¹¹ Y. Fuwa, M. Wakeshima and Y. Hinatsu, *J. Phys. Cond. Matt.* **22**, 346003 (2010).
¹² Y. Fuwa, T. Endo, M. Wakeshima, Y. Hinatsu and K. Ohoyama, *J. Am. Chem. Soc.* **132**, 18020 (2010).
¹³ E. E. McCabe, D. G. Free, B. G. Mendis, J. S. Higgins and J. S. O. Evans, *Chem. Mater.* **22**, 6171 (2010).
¹⁴ N. Ni, E. Climent-Pascual, S. Jia, Q. Huang and R. J. Cava, *Phys. Rev. B* **82**, 214419 (2010).
¹⁵ R. H. Liu, J. S. Zhang, P. Cheng, X. G. Luo, J. J. Ying, Y. J. Yan, M. Zhang, A. F. Wang, Z. J. Xiang, G. J. Ye and X. H. Chen, *Phys. Rev. B* **83**, 174450 (2011).
¹⁶ D. G. Free, N. D. Withers, P. J. Hickey and J. O. Evans, *Chem. Mater.* **23**, 1625 (2011).
¹⁷ C. D. Ling, J. E. Millburn, J. F. Mitchell, D. N. Argyriou, J. Linton and H. N. Bordallo, *Phys. Rev. B* **62**, 15096 (2000).
¹⁸ U. Löw, V. J. Emery, K. Fabricius and S. A. Kivelson, *Phys. Rev. Lett.* **72**, 1918 (1994).
¹⁹ T. Yildirim, *Phys. Rev. Lett.* **101**, 057010 (2008).
²⁰ Q. Si and E. Abrahams, *Phys. Rev. Lett.* **101**, 076401 (2008).
²¹ M. J. Han, Q. Yin, W. E. Pickett and S. Y. Savrasov, *Phys. Rev. Lett.* **102**, 107003 (2009).
²² S. Li, C de la Cruz, Q. Huang, Y. Chen, J. W. Lynn, J. Hu, Y. L. Huang, F. C. Hsu, K. W. Yeh, M. K. Wu and P. C. Dai, *Phys. Rev. B* **79**, 054503 (2009).
²³ B. Hunter, *Int. Un. of Cryst. Comm. Newsletter* **20** (1998).
²⁴ A. C. Larson, and R. B. Von Dreele, General structure analysis system, Report No. LAUR-86-748, Los Alamos National Laboratory, Los Alamos, NM, (2000).
²⁵ B. H. Toby, *J. Appl. Crystallogr.* **34** 201 (2001).
²⁶ R. A. Brand, WinNormos Mössbauer fitting program, Universität Duisburg 2008
²⁷ I. D. Brown and D. Altermatt, *Acta Crystallogr. Sect. B* **41**, 244 (1985).
²⁸ N. E. Brese and M. O'Keefe, *Acta Crystallogr. Sect. B* **47**, 192 (1991).
²⁹ P. Blaha, K. Schwarz, G. Madsen, D. Kvasnicka, and J. Luitz, "Wien2k, an augmented plane wave + local orbitals program for calculating crystal properties," (Karlheinz Schwarz, Techn. Universität Wien, Austria), 2001. ISBN

3-9501031-1-2.

- ³⁰ F. Tran, P. Blaha, K. Schwarz, and P. Novák, Phys. Rev. B **74**, 155108 (2006).
- ³¹ F. Yayoi, W. Makoto, and H. Yukio, J. Phys.: Condens. Matter **22**, 346003 (2010).
- ³² S. Fujimoto, Phys. Rev. Lett. **89**, 226402 (2002).
- ³³ S. Fujimoto, Phys. Rev. B **67**, 235102 (2003).